IEEJ Journal of Industry Applications
Vol.4 No.5 pp.593–601 DOI: 10.1541/ieejjia.4.593

Paper

Generalized Modeling and Optimization of a Bidirectional Dual Active Bridge DC–DC Converter Including Frequency Variation

Felix Jauch[*a)] Non-member, Jürgen Biela[*] Non-member

(Manuscript received July 25, 2014, revised Jan. 26, 2015)

The paper presents a novel modeling approach of the power flow in a bidirectional dual active bridge DC–DC converter. By using basic superposition principles, the mathematical distinction of cases is avoided in the modeling process of the high-frequency transformer currents for different types of modulation. The generalized model is used in the optimization of the converter losses of a 3.3 kW electric vehicle battery charger with an input voltage of 400 V and a battery voltage range from 280 V to 420 V. Besides the commonly used control variables such as the phase-shift and the clamping intervals, the variation in the switching frequency is also considered in the optimization process. The optimal modulation including the frequency variation leads to an increase in the converter efficiency up to 8.6% using IGBTs and 17.8% using MOSFETs at the most critical point compared to phase-shift modulation at a fixed switching frequency.

Keywords: DC–DC converter, dual active bridge, frequency variation, modeling, optimization

1. Introduction

During the last few decades the environmental impact of petroleum based transportation infrastructure gained more and more significance. Fossil fuel powered vehicles lead to large emissions of CO_2 and other pollutions. In order to reduce those impacts, electric vehicles will play an important role in our future transportation infrastructure as the use of renewable energy sources is constantly increasing.

For charging the batteries of electric vehicles or storage systems in general, suitable power electronic systems are necessary. Usually, a basic two-stage approach comprising a boost power factor correction (PFC) rectifier and a subsequent high-frequency isolated DC–DC converter is used for a charging system connected to the low-voltage AC grid. Additionally, for implementing vehicle-to-grid (V2G) concepts, the converter systems feature bidirectional power flow capability. Suitable DC–DC converters comprise the dual half-bridge (DHB) [(1)], dual active (full-) bridge (DAB) [(2)] or resonant DC–DC converters [(3)].

For the DAB, several modulation methods like phase-shift modulation [(2)], triangular and trapezoidal current mode modulation [(4)] have been investigated. Further adjustments of these methods have been presented in (5). Usually, for each of these modulation methods, piecewise linear equations are used to describe the currents where several mathematical cases depending on the control variables have to be distinguished. A general optimization of the converter losses becomes relatively complex and demands high computational power.

In this paper, a novel generalized modeling approach of the power flow is presented to include all possible modulation methods at once. The general power flow equation is then used in an optimization procedure to find the optimal modulation which leads to the highest converter efficiency over the whole operating range. Besides the commonly used control variables like the phase-shifts and the clamping intervals, also the switching frequency is considered to control a DAB [(6)].

First, in Sect. 2 the DAB converter topology with its modulation methods is introduced. The mathematical derivation of a novel generalized power flow equation depending on the control variables is presented in Sect. 3. Then, Sect. 4 shows the optimization of the converter losses of a DAB prototype system. Finally, the optimal modulation including the frequency variation is compared to the conventional modulation methods with respect to the converter efficiency.

2. Topology and Modulation

In the following, first the topology of the DAB DC–DC converter with its operating principle is shortly explained. Afterwards, commonly used modulation methods with their operating limits are summarized. These are the phase-shift modulation as well as the trapezoidal and the triangular current mode modulation.

2.1 Dual Active Bridge DC–DC Converter Figure 1 shows the converter topology of a DAB DC–DC converter. The converter consists of a primary and a secondary full-bridge with unidirectional switches. The two full-bridges are connected to the windings of a two-winding transformer and generate high-frequency (HF) square-wave voltages with amplitudes of the DC port voltages V_1, V_2. The converter is operated by phase-shift control where the control variables are the clamping intervals ($v_1 = 0$ and/or $v_2 = 0$) and the phase-shifts of the HF voltages. In Fig. 7(a) the basic equivalent circuit of the converter is given where the full-bridges are modeled by HF voltage sources. The primary referred leakage inductance L_σ of the transformer acts as decoupling and energy transfer

a) Correspondence to: Felix Jauch. E-mail: jauchf@ethz.ch
* Laboratory for High Power Electronic Systems, ETH Zurich
Physikstrasse 3, 8092-Zurich, Switzerland

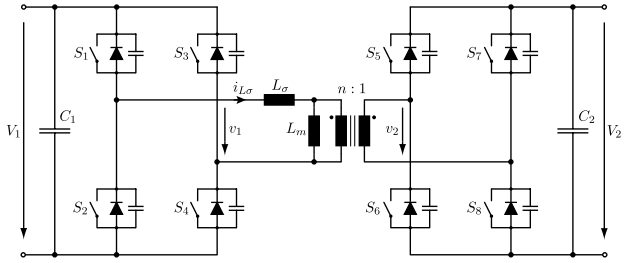

Fig. 1. Topology of the dual active bridge (DAB) DC–DC converter with a primary full-bridge with the switches S_1, S_2, S_3, S_4 and a secondary full-bridge with the switches S_5, S_6, S_7, S_8 connected to a two-winding transformer with leakage inductance L_σ and magnetizing inductance L_m

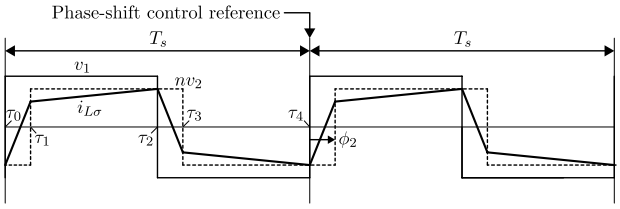

Fig. 2. High-frequency voltages v_1, nv_2 applied to the transformer windings in *phase-shift modulation* and resulting leakage inductance current $i_{L\sigma}$

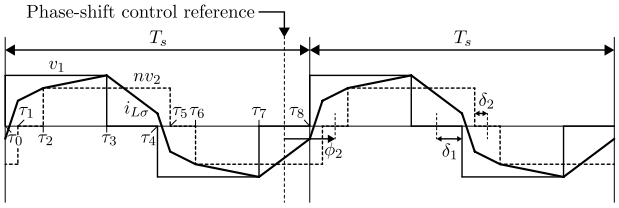

Fig. 3. High-frequency voltages v_1, nv_2 applied to the transformer windings in *general trapezoidal current mode modulation* and resulting leakage inductance current $i_{L\sigma}$

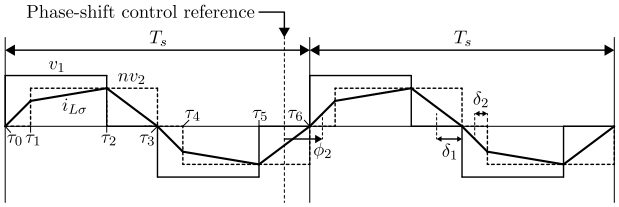

Fig. 4. High-frequency voltages v_1, nv_2 applied to the transformer windings in *trapezoidal current mode modulation* and resulting leakage inductance current $i_{L\sigma}$

element between the square-wave voltages. The magnetizing inductance L_m of the transformer is neglected.

By applying a positive or a negative voltage $v_{L\sigma}$ across the leakage inductance L_σ (see Fig. 7(a)), the current waveform $i_{L\sigma}$ can be controlled during the switching cycle T_s as shown for different modulation methods in Fig. 2, Fig. 3, Fig. 4, Fig. 5, Fig. 6.

2.2 Phase-Shift Modulation In phase-shift modulation, square-wave voltages without clamping intervals are applied to the transformer windings as shown in Fig. 2. The power transferred from the primary to the secondary side is controlled by the phase-shift ϕ_2 between the two voltages v_1, nv_2 and given by

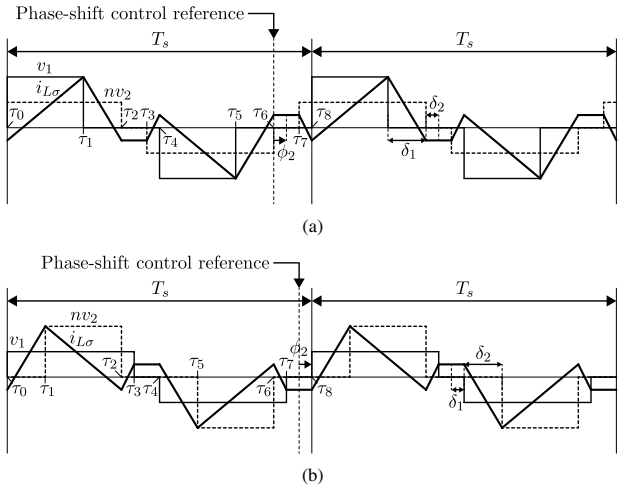

Fig. 5. High-frequency voltages v_1, nv_2 applied to the transformer windings in *general triangular current mode modulation* and resulting leakage inductance current $i_{L\sigma}$ for $V_1 > nV_2$ (a) and $V_1 < nV_2$ (b)

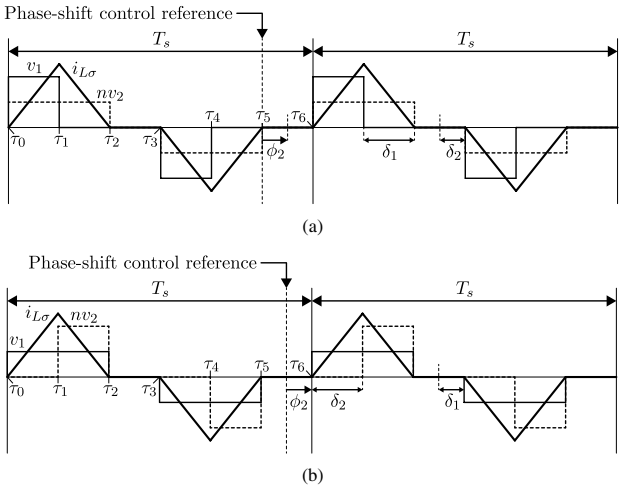

Fig. 6. High-frequency voltages v_1, nv_2 applied to the transformer windings in *triangular current mode modulation* and resulting leakage inductance current $i_{L\sigma}$ for $V_1 > nV_2$ (a) and $V_1 < nV_2$ (b)

$$P_{12} = -\frac{V_1 n V_2 \phi_2 (\pi - |\phi_2|)}{\pi \omega_s L_\sigma} \quad \cdots\cdots (1)$$

with $\phi_2 \in [-\pi, \pi]$. V_1, V_2 are the input and the output voltage, $\omega_s = 2\pi/T_s$ the angular switching frequency, $n = N_1/N_2$ the turns ratio and L_σ the leakage inductance of the transformer. The maximum transferable power is

$$P_{12,max} = \pm\frac{\pi V_1 n V_2}{4\omega_s L_\sigma} \quad \cdots\cdots (2)$$

The soft-switching range of the modulation where zero voltage switching (ZVS) can be achieved is strongly dependent on the voltage ratio V_1/nV_2 as well as the power level P_{12} [(2)]. Especially for voltage ratios $V_1/nV_2 \ll 1$ and $V_1/nV_2 \gg 1$ at low loads, ZVS cannot be maintained. Disadvantages like limited soft-switching range and high RMS transformer currents can be overcome by using the trapezoidal current mode modulation explained in the next section.

2.3 Trapezoidal Current Mode Modulation In trapezoidal current mode modulation, square-wave voltages

with clamping intervals are applied to the transformer windings as shown in Fig. 3 for the general modulation mode. By setting $\tau_0 = \tau_1$ and $\tau_4 = \tau_5$ in Fig. 3 the trapezoidal current mode modulation given in Fig. 4 is obtained. The transferred power is then described by

$$P_{12} = -\text{sign}(\phi_2)\frac{V_1 n V_2(\pi|\phi_2| - 2\phi_2^2 + 2\delta_1\delta_2)}{\pi\omega_s L_\sigma} \cdots\cdots (3)$$

with $\delta_1 = f(\phi_2) \in [0, \pi/2]$, $\delta_2 = f(\phi_2) \in [0, \pi/2]$ and $\phi_2 \in [-\pi, \pi]$. The maximum transferable power is

$$P_{12,max} = \pm\frac{\pi V_1^2 n^2 V_2^2}{2\omega_s L_\sigma (V_1^2 + n^2 V_2^2 + V_1 n V_2)}. \cdots\cdots\cdots (4)$$

The current $i_{L\sigma}$ reaches zero at switching instants τ_0, τ_3, τ_6 where zero current switching (ZCS) is possible [4]. At $\tau_1, \tau_2, \tau_4, \tau_5$ ZVS is possible as far as the minimum commutation current needed for the resonant transition is reached. Nevertheless, the modulation method cannot be applied for low output power. This leads to the triangular current mode modulation with a seamless transition between the modulation methods.

2.4 Triangular Current Mode Modulation In triangular current mode modulation, also square-wave voltages with clamping intervals are applied to the transformer windings as can be seen from Fig. 5 for the general modulation mode. Considering $\tau_3 = \tau_4$ and $\tau_7 = \tau_8$ in Fig. 5(a) as well as $\tau_2 = \tau_3$ and $\tau_6 = \tau_7$ in Fig. 5(b) the triangular current mode modulation shown in Fig. 6 is obtained. The transferred power can then be written as

$$P_{12} = -\frac{V_1 n V_2 \phi_2(\pi - 2\delta_1)}{\pi\omega_s L_\sigma}, \qquad V_1 > nV_2 \cdots\cdots (5)$$

$$P_{12} = -\frac{V_1 n V_2 \phi_2(\pi - 2\delta_2)}{\pi\omega_s L_\sigma}, \qquad V_1 < nV_2 \cdots\cdots (6)$$

with $\delta_1 = f(\phi_2) \in [0, \pi/2]$, $\delta_2 = f(\phi_2) \in [0, \pi/2]$ and $\phi_2 \in [-\pi, \pi]$. The maximum transferable power is

$$P_{12,max} = \pm\frac{\pi n^2 V_2^2 (V_1 - nV_2)}{2\omega_s L_\sigma V_1}, \qquad V_1 > nV_2 \cdots\cdots (7)$$

$$P_{12,max} = \pm\frac{\pi V_1^2 (V_1 - nV_2)}{2\omega_s L_\sigma n V_2}, \qquad V_1 < nV_2. \cdots\cdots (8)$$

The current $i_{L\sigma}$ reaches zero at the switching instants $\tau_0, \tau_2, \tau_3, \tau_5, \tau_6$ where ZCS is possible [4]. At the instants τ_1, τ_4 ZVS is possible. Depending on the voltage ratio, the modulation shown in Fig. 6(a) with $V_1 > nV_2$ or the modulation shown in Fig. 6(b) with $V_1 < nV_2$ is applied. Power transfer in case of $V_1 = nV_2$ is not possible with the triangular current mode.

3. Modeling of Power Flow

For designing and controlling the DAB converter system, the mathematical description of the power flow depending on the control variables is essential. The optimization procedure shown in Fig. 11 requires the calculation of the power flow P_{12} for evaluating the power equality constraint.

The well-known approach uses piecewise linear equations

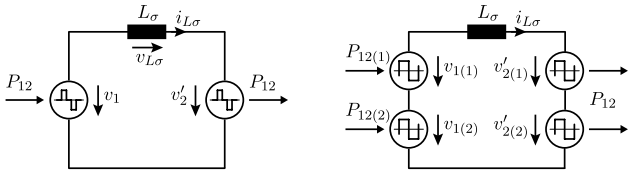

Fig. 7. Simplified circuit of a two-port converter applying square-wave voltages with clamping intervals (a) and the equivalent four-port circuit applying square-wave voltages without clamping intervals at the ports (b)

for the transformer leakage inductance current where several mathematical cases depending on the phase-shifts and the clamping intervals have to be distinguished. Due to the mathematical complexity, especially for high port numbers in multi-port converters [7], the following analysis uses basic superposition principles to find the general analytical formula for the power flow. With this approach, there is no need for mathematical distinction of cases.

The mathematical analysis of the power flow is based on the primary side referred equivalent circuit of the converter topology shown in Fig. 7(a). The full-bridges are modeled by HF square-wave voltage sources v_1, v_2' with clamping intervals as shown in Fig. 7(a).

The power flow over one switching cycle $T_s = 2\pi/\omega_s$ between two ports (from a first port 1 to a second port 2) applying square-wave voltages with clamping intervals as shown in Fig. 7(a) is based on the well-known power flow equation [8] (power from primary port p to secondary port s)

$$P_{ps} = \frac{V_p n V_s}{\omega_s L_\sigma}\left(\phi_p - \phi_s\right)\left(1 - \frac{\left|\phi_p - \phi_s\right|}{\pi}\right). \cdots\cdots\cdots (9)$$

There, two square-wave voltages with 50% duty cycles, amplitudes V_p, V_s and phases $\phi_p, \phi_s \in [-\pi, \pi]$ are applied across the windings of a two-winding transformer with primary referred leakage inductance L_σ, negligible large magnetizing inductance and turns ratio $n = N_p/N_s$. The phase angles are measured against a given reference, a positive angle defines a leading signal and a negative angle a lagging signal with respect to the reference.

The two-port circuit with clamping intervals given in Fig. 7(a) can be modeled by the equivalent four-port circuit shown in Fig. 7(b) where only square-wave voltages without clamping intervals and duty cycles of 50% occur. This is done by splitting up the voltage v_1 with clamping interval into a sum $v_{1(1)} + v_{1(2)}$ of two voltages with 50% duty cycle, no clamping interval and a phase-shift of $2\delta_1$ against each other as depicted in Fig. 8. Analogously, this is done for the voltage v_2. The power transferred from port 1 to port 2 is then given by

$$P_{12} = \underbrace{\frac{1}{T_s}\int_0^{T_s} v_{1(1)} i_{L\sigma}\, d\tau}_{P_{12(1)}} + \underbrace{\frac{1}{T_s}\int_0^{T_s} v_{1(2)} i_{L\sigma}\, d\tau}_{P_{12(2)}} \cdots\cdots (10)$$

with the two power shares of voltage sources $v_{1(1)}, v_{1(2)}$ (see Fig. 7(b)).

Since the voltage-second product of each source in Fig. 7(b) over a switching cycle T_s is zero, a single source only delivers reactive power to the leakage inductance L_σ. Therefore, the calculation of the power share $P_{12(1)}$ can be done by splitting up the leakage inductance current $i_{L\sigma}$ into three parts $i_{L\sigma(I)}, i_{L\sigma(II)}, i_{L\sigma(III)}$ which are obtained by applying the superposition principle as shown in Fig. 9 by selectively short-circuiting voltage sources. In this way, the active power exchange of source $v_{1(1)}$ with sources $v_{1(2)}, v'_{2(1)}, v'_{2(2)}$ is described. Although the source $v_{1(1)}$ contributes three times to the current $i_{L\sigma}$ by applying the proposed superposition, this current part cancels out in the active power calculation, as it only describes reactive power delivered from $v_{1(1)}$ to L_σ. Compared to conventional superposition the current driven by $v_{1(1)}$ is increased by a factor of 3, nevertheless it does not contribute to the active power calculation.

The power share $P_{12(1)}$ in (10) can then be written as

$$P_{12(1)} = \underbrace{\frac{1}{T_s}\int_0^{T_s} v_{1(1)} i_{L\sigma(I)}\, d\tau}_{P_{12(1)(I)}} + \underbrace{\frac{1}{T_s}\int_0^{T_s} v_{1(1)} i_{L\sigma(II)}\, d\tau}_{P_{12(1)(II)}} + \underbrace{\frac{1}{T_s}\int_0^{T_s} v_{1(1)} i_{L\sigma(III)}\, d\tau}_{P_{12(1)(III)}}. \tag{11}$$

Analogously, the second power share $P_{12(2)}$ is described. From Fig. 9 and (11) it is concluded, that the power shares

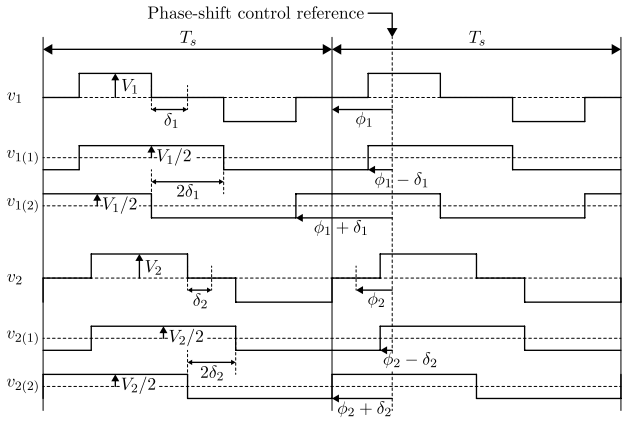

Fig. 8. Square-wave voltages v_1, v_2 with the clamping intervals $2\delta_1, 2\delta_2$ and the underlying square-wave voltages $v_{1(1)}, v_{1(2)}, v_{2(1)}, v_{2(2)}$ without clamping intervals and duty cycles 50% which add up to v_1 and v_2 respectively

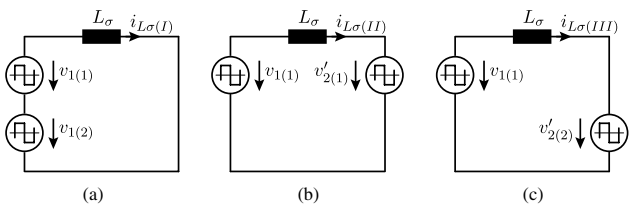

Fig. 9. Leakage inductance current obtained for power calculation by applying the superposition principle with three parts (a), (b), (c) by selectively short-circuiting voltage sources: $i_{L\sigma} = i_{L\sigma(I)} + i_{L\sigma(II)} + i_{L\sigma(III)}$

$P_{12(1)(I)}, P_{12(1)(II)}, P_{12(1)(III)}$ are given by (9). This is also the case for the power shares $P_{12(2)(I)}, P_{12(2)(II)}, P_{12(2)(III)}$. By summing up all the power shares, the resulting power transferred per switching cycle from port 1 to port 2 applying the square-wave voltages v_1, v_2 with the clamping intervals $2\delta_1, 2\delta_2$ and the phases ϕ_1, ϕ_2 as shown in Fig. 8 is thus given as

$$\begin{aligned} P_{12} = \frac{V_1 n V_2}{4\omega_s L_\sigma}\Bigg[& ((\phi_1-\delta_1)-(\phi_2-\delta_2))\left(1-\frac{|(\phi_1-\delta_1)-(\phi_2-\delta_2)|}{\pi}\right) \\ & + ((\phi_1-\delta_1)-(\phi_2+\delta_2))\left(1-\frac{|(\phi_1-\delta_1)-(\phi_2+\delta_2)|}{\pi}\right) \\ & + ((\phi_1+\delta_1)-(\phi_2-\delta_2))\left(1-\frac{|(\phi_1+\delta_1)-(\phi_2-\delta_2)|}{\pi}\right) \\ & + ((\phi_1+\delta_1)-(\phi_2+\delta_2))\left(1-\frac{|(\phi_1+\delta_1)-(\phi_2+\delta_2)|}{\pi}\right)\Bigg]. \end{aligned} \tag{12}$$

In general, the proposed superposition method for deriving analytical power flow equations can be applied to any number of ports which are connected in series in multi-port converters as for instance shown in (9) for an isolated three-phase bidirectional AC–DC converter.

4. Optimization of Converter Losses

The general power flow Eq. (12) is used in an optimization of converter losses of a DAB prototype system designed for a nominal output power of 3.3 kW. The loss model includes the main loss shares as conduction and switching losses of the semiconductor devices, skin and proximity effect losses of the transformer windings as well as the core losses of the transformer.

4.1 Prototype System As a prototype system to find optimal control variables, a 3.3 kW electric vehicle battery charger to connect to a fixed 400 V DC-link with an output voltage range of 280 V to 420 V of a lithium-ion battery is considered. The primary and secondary switching devices are chosen to be 650 V IGBTs of type IKW50N65F5 for a first converter solution and 650 V MOSFETs of type IPW65R019C7 for a second converter solution, both from Infineon [10]. The system parameters are listed in detail in Table 1.

4.2 Loss Models For optimizing the DAB converter system, its main losses occurring in the semiconductor devices as well as in the transformer have to be modeled. For the semiconductor devices, both IGBT and MOSFET loss models based on datasheet parameters are used and given in the following.

Table 1. Parameters of the prototype system

Input voltage	V_1	400 V
Battery voltage	V_2	280 V…420 V
Output power	P_2	3.3 kW
Switching frequency	f_s	20 kHz…50 kHz
Transformer turns ratio	n	8/7
Transformer leakage inductance	L_σ	
Phase-shift modulation	$L_{\sigma(1)}$	181 µH
Triangular/Trapezoidal current modulation	$L_{\sigma(2)}$	158 µH
Optimized control variables modulation	$L_{\sigma(3)}$	158 µH
Transformer magnetizing inductance	L_m	neglected

4.2.1 IGBT Losses For calculating the conduction losses, the typical output characteristic $i_C = f(v_{CE})$ of the IGBT and the typical diode forward current as a function of the forward voltage $i_D = f(v_D)$ of the anti parallel diode at a junction temperature of $T_{j,max} - 25\,°\mathrm{C} = 150\,°\mathrm{C}$ from the datasheet are considered. Given the current i_C flowing through the IGBT and the current i_D through the diode over the interval $[0, T_s]$ of a switching period, the conduction losses of an IGBT co-pack device can be calculated by

$$P_{c,S} = \frac{1}{T_s}\int_0^{T_s} i_C(\tau)\cdot v_{CE}(i_C(\tau))\,d\tau, \cdots\cdots\cdots\cdots (13)$$

$$P_{c,D} = \frac{1}{T_s}\int_0^{T_s} i_D(\tau)\cdot v_D(i_D(\tau))\,d\tau, \cdots\cdots\cdots\cdots (14)$$

$$P_c = P_{c,S} + P_{c,D}. \cdots\cdots\cdots\cdots\cdots\cdots\cdots\cdots (15)$$

When optimizing and designing a converter system, the details of the gate drives and the parasitics of the commutation path are usually unknown, so that only approximations of the switching losses can be performed. For estimating the switching losses of an IGBT co-pack device, the following assumptions are made: For a device which is turned on

- the diode losses at zero-voltage turn-on are neglected,
- the IGBT losses $E_{on} = f(i_C)$ at turn-on including the diode reverse recovery losses are taken from the datasheet and are linearly scaled with the voltage according to the datasheet.

For a device which is turned off

- the diode losses at turn-off are neglected,
- the IGBT losses $E_{off} = f(i_C)$ at turn-off are taken from the datasheet and are linearly scaled with the voltage according to the datasheet.

For soft-switching in terms of ZVS at the switching instant τ_s, the switching losses of an IGBT co-pack device are approximated by

$$P_s = f_s \cdot E_{off}(i_C(\tau_s))\frac{v_{CE}(\tau_s)}{V_{CE}}, \cdots\cdots\cdots\cdots\cdots (16)$$

whereas for hard-switching in terms of forced diode commutation, the switching losses are estimated according to

$$P_s = f_s \cdot E_{on}(i_C(\tau_s))\frac{v_{CE}(\tau_s)}{V_{CE}} \cdots\cdots\cdots\cdots\cdots (17)$$

with V_{CE} being the collector-emitter voltage where the switching losses were measured according to the datasheet. For soft-switching in terms of ZCS for a small $i_C(\tau_s)$, the losses according to (16) and (17) become negligible small.

4.2.2 MOSFET Losses Also for MOSFETs, the typical output characteristic $i_D = f(v_{DS})$ at a junction temperature of $T_{j,max} - 25\,°\mathrm{C} = 125\,°\mathrm{C}$ from the datasheet can be used to calculate the conduction losses. Given the current i_D flowing through the MOSFET over the interval $[0, T_s]$ of a switching period, the conduction losses are given by

$$P_c = \frac{1}{T_s}\int_0^{T_s} i_D(\tau)\cdot v_{DS}(i_D(\tau))\,d\tau. \cdots\cdots\cdots\cdots (18)$$

The approximation of the switching losses of a MOSFET device is based on the following assumptions: For ZVS conditions when stored energy in the output capacitance is transferred from one MOSFET to another, the difference between released and absorbed energy is negligible small. In other words, the losses during the commutation of the inductive current are neglected, $P_s = 0$. For hard-switching, two loss effects are modeled, these are

- the dissipation of the energy $E_{oss} = f(v_{DS})$ stored in the output capacitance at turn-on,
- the body diode reverse recovery losses occurring in the turn-on device squarely scaled with the voltage and linearly scaled with the current [11].

The switching losses at the time instant τ_s are then estimated using

$$P_{oss} = f_s \cdot E_{oss}(v_{DS}(\tau_s)), \cdots\cdots\cdots\cdots\cdots\cdots (19)$$

$$P_{rr} = f_s \cdot Q_{rr}\left(\frac{v_{DS}(\tau_s)}{V_R}\right)^2 \frac{i_D(\tau_s)}{I_F}\cdot v_{DS}(\tau_s), \cdots\cdots (20)$$

$$P_s = P_{oss} + P_{rr}, \cdots\cdots\cdots\cdots\cdots\cdots\cdots\cdots (21)$$

with the curve $E_{oss} = f(v_{DS})$ and the reverse recovery charge Q_{rr} measured for the reverse voltage V_R and the forward current I_F from the datasheet. For soft-switching in terms of ZCS for a small $i_D(\tau_s)$, the losses according to (20) become negligible small, hence the losses are mainly described by (19).

4.2.3 Transformer Losses Besides the losses in the semiconductor devices, the transformer losses in terms of core and winding losses are modeled. The transformer is built with four U-cores of the size AMCC-32 [12] with the material VITROPERM 500F [13] which exhibits a relatively high saturation flux density of 1.2 T and is therefore ideally suited for switching frequencies in the range of a few 10 kHz. For the windings, litz wire with 945 strands of diameter 0.071 mm is used. On the primary side, there are 24 turns, whereas the secondary winding consists of 21 turns. The primary winding W_1 is directly wound on the inner leg with the secondary winding W_2 around the inner leg and the outer leakage leg as shown in Fig. 10. By inserting an air gap of length δ_σ in the leakage leg, the leakage inductance L_σ can be set. Practically, distributed air gaps are used in order to reduce the

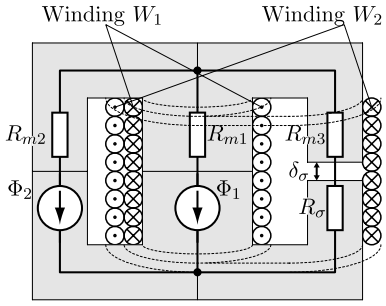

Fig. 10. 2D drawing of the transformer including reluctance model consisting of four U-cores with the primary winding W_1 wound around the inner leg and the secondary winding W_2 around the inner and the right-hand sided leakage leg. By inserting an air gap of length δ_σ in the leakage leg, the leakage inductance L_σ can be set

Table 2. Transformer parameters of the prototype system

Magnetic core	2x AMCC-32 VITROPERM 500F
Primary winding W_1	24 turns, litz wire 945 strands, 0.071 mm
Secondary winding W_2	21 turns, litz wire 945 strands, 0.071 mm
Air gap length δ_σ	
Phase-shift modulation	1.6 mm
Triangular/Trapezoidal current modulation	1.8 mm
Optimized control variables modulation	1.8 mm

losses induced by the fringing magnetic field. The leakage inductance L_σ is determined in such a way, that the maximum input power of 3.3 kW can be transferred at the lowest switching frequency of 20 kHz and the lowest battery voltage of 280 V for the considered modulation method. The transformer parameters are summarized in Table 2.

In the loss model, the core losses per volume are calculated by applying the improved generalized Steinmetz equation (iGSE) [14]. The skin and proximity effect losses per unit length in litz wires for each current harmonic are determined according to (15). The external magnetic field strength for evaluating proximity effect losses is derived by a 1D approximation using the Dowell method [16].

4.2.4 Auxiliary Losses Besides the load dependent loss shares shown in the previous sections, a constant loss share for gate drives, control, sensing and fans of 8 W is considered.

4.3 Optimization Procedure The optimal control variables in terms of the clamping intervals δ_1, δ_2, the phase-shift ϕ_2 and the switching frequency f_s are numerically determined by minimizing the total converter losses (semiconductor losses P_{sw}, transformer losses P_{tr} and auxiliary losses P_{aux}) subject to the power flow constraint. The optimization procedure is shown in Fig. 11. For a given output voltage $V_2 \in [280\,\mathrm{V}, 420\,\mathrm{V}]$ and a reference output power $P_{12}^* \in [0.33\,\mathrm{kW}, 3.3\,\mathrm{kW}]$, the optimization routine calculates the optimal control variables. The optimization problem is stated as

$$\min_x \left[P_{sw} + P_{tr} + P_{aux}\right] \text{ with respect to } x = \begin{bmatrix}\delta_1\\ \delta_2\\ \phi_2\\ f_s\end{bmatrix} \cdots (22)$$

with

$$x_{lb} = \begin{bmatrix}0\\ 0\\ -\pi\\ 20\,\mathrm{kHz}\end{bmatrix},\ x_{ub} = \begin{bmatrix}\pi/2\\ \pi/2\\ \pi\\ 50\,\mathrm{kHz}\end{bmatrix} \cdots\cdots\cdots\cdots\cdots (23)$$

where x denotes the vector of control variables which is restricted to the lower and upper bounds x_{lb}, x_{ub} respectively. The equality constraint is given by setting the power transfer $P_{12} = P_{12}^*$ using (12).

4.4 Optimization Results The calculated relative converter efficiencies applying the phase-shift modulation, the combined triangular/trapezoidal current mode modulation and the modulation with optimized control variables including frequency variation are shown in Fig. 12 and Table 3 for an IGBT solution and in Fig. 13 and Table 4 for a MOSFET solution.

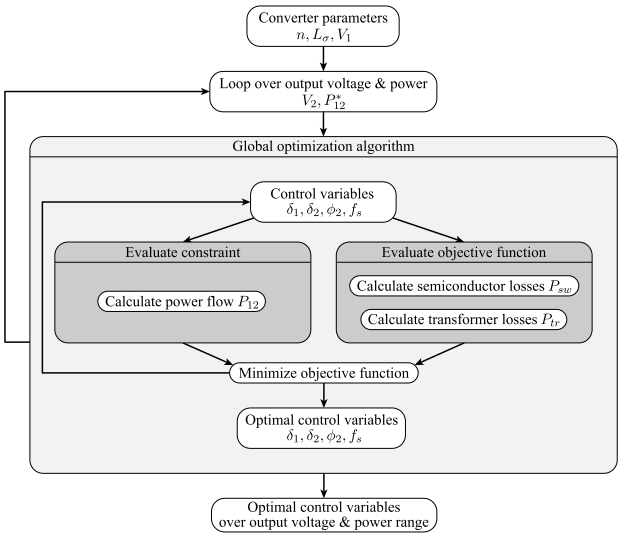

Fig. 11. Visualization of the optimization procedure to find the optimal control variables $\delta_1, \delta_2, \phi_2, f_s$ by minimizing the DAB converter losses subject to the power flow constraint. P_{12}^* represents the reference value for the transferred power

Table 3. Efficiencies for different modulation methods applying IGBTs. Average efficiency is calculated over the whole output voltage/power range

Modulation method	Calculated efficiency	
	Peak	Average
Phase-shift modulation	98.0%	96.9%
Triangular/Trapezoidal current modulation	98.2%	97.5%
Optimized control variables modulation	98.2%	97.6%

Table 4. Efficiencies for different modulation methods applying MOSFETs. Average efficiency is calculated over the whole output voltage/power range

Modulation method	Calculated efficiency	
	Peak	Average
Phase-shift modulation	99.0%	97.6%
Triangular/Trapezoidal current modulation	99.0%	98.3%
Optimized control variables modulation	99.1%	98.5%

For the phase-shift modulation, it can be seen that for the MOSFET solution in the soft-switching area higher efficiencies are achieved than for the IGBT solution (compare Fig. 13a to Fig. 12a). This is mainly due to the fact, that IGBT turn-off losses cannot be substantially reduced by using ZVS. In the hard-switching region, ZVS is lost and forced diode commutations occur. The switching losses in this region are strongly dependent on the characteristics of the anti parallel diode of the IGBT and the body diode of the MOSFET respectively.

To improve the efficiencies, especially in the hard-switching region, the combined triangular/trapezoidal current mode modulation can be used. There, also for a low output power in the areas of low and high output voltages, soft-switching (ZCS combined with ZVS) can be achieved.

Considering also the frequency variation, the efficiencies can be slightly increased compared to the triangular/

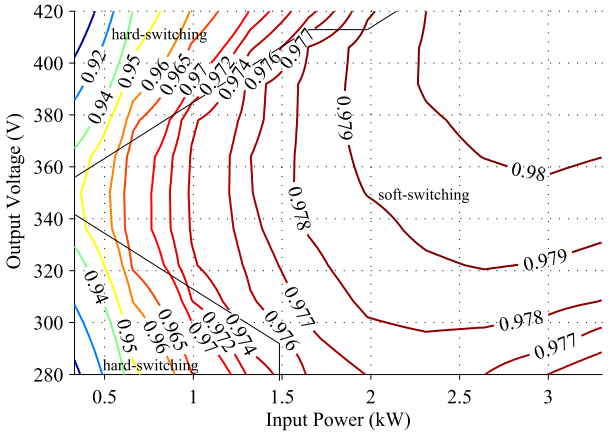

(a)

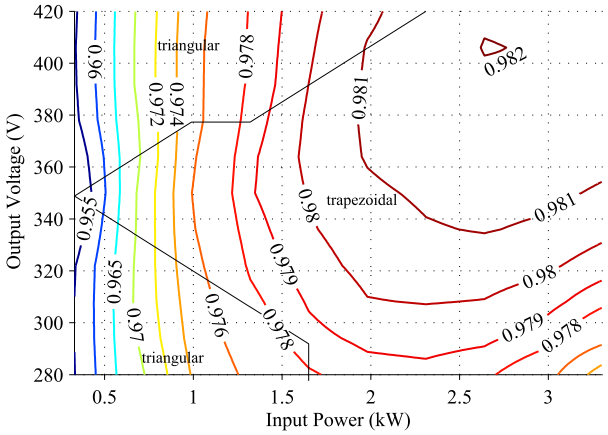

(b)

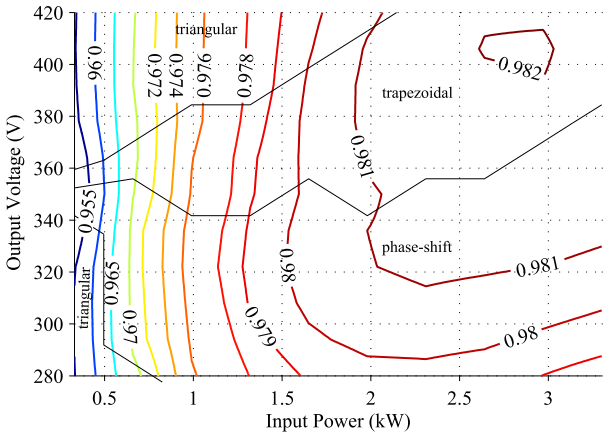

(c)

Fig. 12. Relative converter efficiencies applying IGBTs for an input power range of 10% to 100% of maximum input power and an output voltage range of 280 V to 420 V for the phase-shift modulation (a) and the triangular/trapezoidal current mode modulation (b) both with fixed switching frequency at 20 kHz and for the modulation with optimized control variables with variable switching frequency from 20 kHz to 50 kHz (c). For the phase-shift modulation in (a), soft- and hard-switching areas are given, whereas with the modulations in (b) and (c) soft-switching is always achieved. In (c), also the modulation mode found by the optimization is given

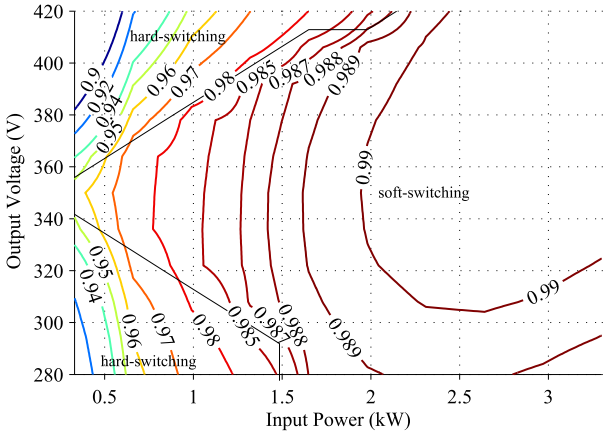

(a)

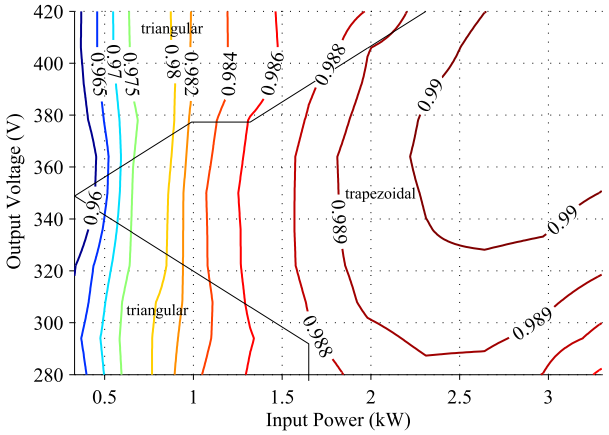

(b)

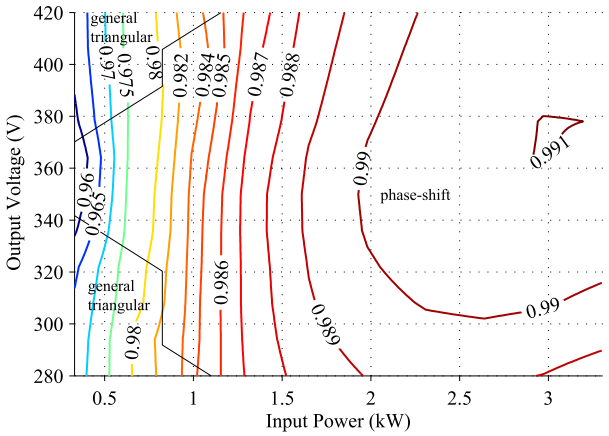

(c)

Fig. 13. Relative converter efficiencies applying MOSFETs for an input power range of 10% to 100% of maximum input power and an output voltage range of 280 V to 420 V for the phase-shift modulation (a) and the triangular/trapezoidal current mode modulation (b) both with fixed switching frequency at 20 kHz and for the modulation with optimized control variables with variable switching frequency from 20 kHz to 50 kHz (c). For the phase-shift modulation in (a), soft- and hard-switching areas are given, whereas with the modulations in (b) and (c) soft-switching is always achieved. In (c), also the modulation mode found by the optimization is given

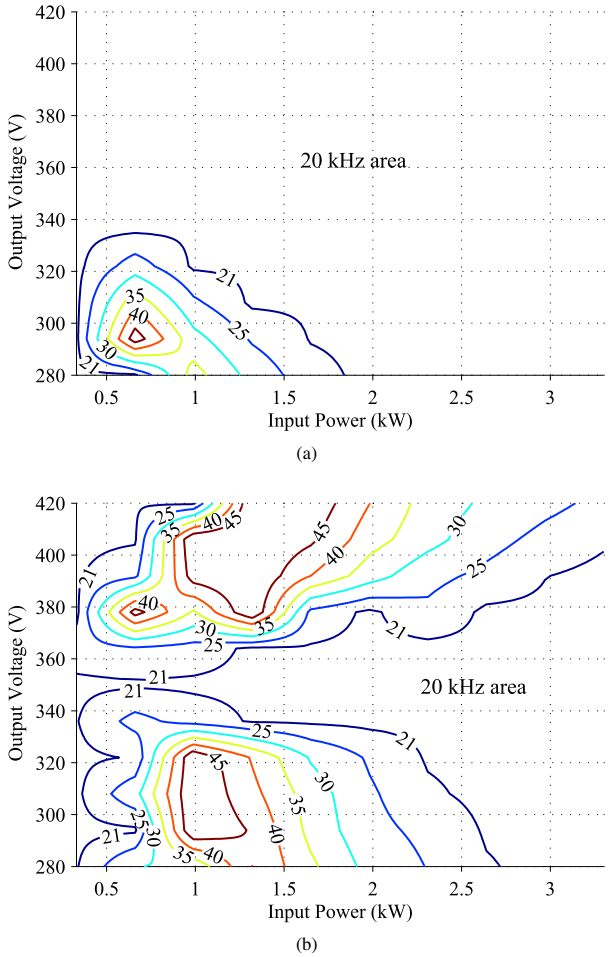

Fig. 14. Switching frequencies in kHz for the optimized control variables modulation for an input power range of 10% to 100% of maximum input power and an output voltage range of 280 V to 420 V using IGBTs (a) and using MOSFETs (b)

trapezoidal current mode modulation. Soft-switching is achieved in the whole operating range: ZCS and ZVS for the IGBT solution and only ZVS for the MOSFET solution. The modulation modes, which are found by the optimization procedure, are given in Fig. 12c and Fig. 13c. Figure 14 shows the resulting switching frequencies found by the optimization, both for the IGBT and the MOSFET solution. Especially for the MOSFET solution, the frequency is varied over a wide area of the operating range. With decreasing power, the frequency can be increased to lower the power transfer and to achieve high efficiencies at the same time. Nevertheless, at low input powers, it is more attractive to decrease the switching frequency and change the modulation mode when necessary (see Fig. 13c).

For a 14.2 kWh battery pack with 11.5 Ah lithium iron phosphate ($LiFePO_4$) cells [17], the efficiencies of a typical charging process from 10% to 90% state-of-charge (battery voltage from 385 V to 418 V) with a constant input power of $P_1 = 3.3$ kW are calculated and given in Table 5 for the different modulation methods applying IGBTs and MOSFETs. It can be seen, that the charging efficiencies at the maximum input power do not differ much for the same semiconductor technology applying different modulation methods.

Table 5. Charging efficiencies of a 14.2 kWh lithium-ion battery pack from 10% to 90% state-of-charge for different modulation methods applying IGBTs and MOSFETs

Modulation method	Charging efficiency	
	IGBTs	MOSFETs
Phase-shift modulation	98.0%	99.0%
Triangular/Trapezoidal current modulation	98.1%	99.0%
Optimized control variables modulation	98.1%	99.0%

5. Conclusion

A novel modeling approach of the power flow in a bidirectional DAB DC–DC converter is presented. By using basic superposition principles, the mathematical distinction of cases is avoided in the modeling process of the HF transformer currents for different types of modulations. The generalized model is used in an optimization of the converter losses for an IGBT and a MOSFET solution considering all types of modulations, also including the variation of frequency for the converter control. For a 3.3 kW electric vehicle battery charger, the efficiency increases up to 8.6% using IGBTs and 17.8% using MOSFETs at the most critical point compared to phase-shift modulation at a fixed switching frequency.

Acknowledgment

The authors would like to thank Swisselectric Research and the Competence Center Energy and Mobility (CCEM) very much for their strong financial support of the research work.

References

(1) H. Fan and H. Li: “High Frequency High Efficiency Bidirectional DC–DC Converter Module Design for 10 kVA Solid State Transformer”, in Proc. 25th Applied Power Electronics Conference and Exposition (APEC), pp.210–215 (2010)
(2) M.N. Kheraluwala, R.W. Gascoigne, D.M. Divan, and E.D. Baumann: “Performance Characterization of a High-Power Dual Active Bridge DC-to-DC Converter”, *IEEE Trans. on Ind. Appl.*, Vol.28, No.6, pp.1294–1301 (1992)
(3) R.L. Steigerwald: “A comparison of half-bridge resonant converter topologies”, *IEEE Trans. Power Electron.*, Vol.3, No.2, pp.174–182 (1988)
(4) N. Schibli: “Symmetrical multilevel converters with two quadrant DC–DC feeding”, Ph.D. dissertation, Swiss Federal Institute of Technology Lausanne (EPFL) (2000)
(5) F. Krismer: “Modeling and Optimization of Bidirectional Dual Active Bridge DC–DC Converter Topologies”, Ph.D. dissertation, ETH Zurich (2010)
(6) G. Guidi, M. Pavlovsky, A. Kawamura, T. Imakubo, and Y. Sasaki: “Improvement of light load efficiency of Dual Active Bridge DC–DC converter by using dual leakage transformer and variable frequency”, in Proc. Energy Conversion Congress and Exposition (ECCE), pp.830–837 (2010)
(7) F. Jauch and J. Biela: “An Innovative Bidirectional Isolated Multi-Port Converter with Multi-Phase AC Ports and DC Ports”, in Proc. 5th EPE Joint Wind Energy and T&D Chapters Seminar (2012)
(8) A.M. Ari, L. Li, and O. Wasynczuk: “Modeling and Analysis of N-Port DC–DC Converters using the Cyclic Average Current”, in Proc. 27th Applied Power Electronics Conference and Exposition (APEC), pp.863–869 (2012)
(9) F. Jauch and J. Biela: “Modelling and ZVS control of an isolated three-phase bidirectional AC–DC converter”, in Proc. 15th European Conference on Power Electronics and Applications (EPE), pp.1–11 (2013)
(10) [Online]. Available: http://www.infineon.com
(11) N. Mohan, T.M. Undeland, and W.P. Robbins: Power Electronics: Converters, Applications, and Design, John Wiley & Sons (2002)
(12) [Online]. Available: http://www.hitachi-metals.co.jp
(13) [Online]. Available: http://www.vacuumschmelze.de
(14) K. Venkatachalam, C. Sullivan, T. Abdallah, and H. Tacca: “Accurate Prediction of Ferrite Core Loss with Nonsinusoidal Waveforms using only

Steinmetz Parameters", in Proc. 8th IEEE Workshop on Computers in Power Electronics, pp.36–41 (2002)
(15) J. Mühlethaler, "Modeling and Multi-Objective Optimization of Inductive Power Components", Ph.D. dissertation, ETH Zurich (2012)
(16) P. Dowell: "Effects of Eddy Currents in Transformer Windings", Proc. of the Institution of Electrical Engineers, Vol.113, No.8, pp.1387–1394 (1966)
(17) A. Vezzini: "Lithiumionen-Batterien als Speicher für Elektrofahrzeuge, Teil 1: Technische Möglichkeiten heutiger Batterien", Bulletin SEV/AES, Vol.3, pp.19–23 (2009)

Felix Jauch (Non-member) Felix Jauch was born 1986 in Baden, Switzerland. He studied electrical engineering and information technology at the Swiss Federal Institute of Technology (ETH) in Zurich. During his studies he focused on power electronics, electrical drives and electric power systems. After he had received his bachelor's degree in August 2008, he worked at Bombardier Transportation Switzerland as an intern where he developed electronic equipment for a test environment for traction converters. His master thesis dealt with developing a test environment for high frequency converter for ultra-high-speed electrical drive systems and was carried out with the ETH spin-off company Celeroton. In October 2010 he received his master's degree. Since January 2011, he joined the Laboratory for High Power Electronic Systems as a PhD student focusing on fast charging stations for electric vehicles.

Jürgen Biela (Non-member) (S'04M'06) received the Diploma (Hons.) degree from Friedrich-Alexander-Universitaet, Erlangen-Nuernberg, Nuremberg, Germany, and the Ph.D. degree from the Swiss Federal Institute of Technology (ETH) Zurich, Zurich, Switzerland, in 1999 and 2006, respectively. He dealt, in particular, with resonant dc-link inverters with the University of Strathclyde, Glasgow, U.K., and the active control of series-connected IGCTs with the Technical University of Munich, Munich, Germany, during his studies. In 2000, he joined the Research Department, Siemens Automation and Drives, Erlangen, Germany, where he was involved in inverters with very high switching frequencies, SiC components, and EMC. In 2002, he joined the Power Electronic Systems Laboratory (PES), ETH Zurich, for working toward the Ph.D. degree, focusing on optimized electromagnetically integrated resonant converters. From 2006 to 2007, he was a Post-Doctoral Fellow with PES and a Guest Researcher with the Tokyo Institute of Technology, Tokyo, Japan. From 2007 to 2010, he was a Senior Research Associate with PES. Since 2010, he has been an Associate Professor in high-power electronic systems with ETH Zurich. His current research interests include the design, modeling, and optimization of PFC, dcdc and multilevel converters with emphasis on passive components, and the design of pulsed-power systems and power electronic systems for future energy distribution.